MASCS 1.0: Synchronous atmospheric and oceanic data from a cross-shaped moored array in the northern South China Sea during 2014–2015

Han Zhang[1,2,3], Dake Chen[1,2,4], Tongya Liu[1,2], Di Tian[1], Min He[2], Qi Li[2], Guofei Wei[6,7], Jian Liu[2,5]

[1] State Key Laboratory of Satellite Ocean Environment Dynamics, Second Institute of Oceanography, Ministry of Natural Resources, Hangzhou 310012, China

[2] Southern Marine Science and Engineering Guangdong Laboratory (Zhuhai), Zhuhai 519082, China

[3] State Key Laboratory of Marine Environmental Science, Xiamen University, Xiamen 361102, China

[4] School of Oceanography, Shanghai Jiao Tong University, Shanghai 200030, China

[5] School of Geography and Ocean Science, Ministry of Education Key Laboratory for Coast and Island Development, Nanjing University, Nanjing 210023, China

[6] Key Laboratory of Straits Severe Weather China Meteorological Administration, Fuzhou 350028, China

[7] Fujian Meteorological Observatory, Fuzhou 350028, China

Correspondence: Han Zhang (zhanghan@sio.org.cn)

Abstract. This work presents a cross-shaped moored array dataset (MASCS 1.0) comprising five buoys and four moorings with synchronous atmospheric and oceanic data in the northern South China Sea during 2014–2015. The atmospheric data are observed by two meteorological instruments at the buoys. The oceanic data consist of sea surface waves measured using a wave recorder, temperature, and salinity from the surface to a depth of 400 m, and at 10 and 50 m above the ocean bottom using conductivity, temperature, and depth recorders. It also includes currents from the surface to a depth of 850 m measured using acoustic Doppler current profilers and measured at 10, 50, and 100 m above the floor using current meters. Additional measurements were taken for sea surface radiation, air visibility, chlorophyll, turbidity, and chromophoric dissolved organic matter at buoy 3, located at the center of the moored array. The data reveals air–sea interactions and oceanic processes in the upper and bottom ocean, especially the transition of the air–sea interface and ocean conditions from summer to winter monsoon and the effects of six tropical cyclones on the moored array. Multiscale processes were also recorded, such as air–sea fluxes, tides, internal waves, and low-frequency flows. The data are valuable and have many potential applications, including analyzing the phenomena and mechanisms of air–sea interactions and ocean dynamics and validating and improving numerical

model simulations, data reanalysis, and assimilations. All the data described here are made publicly available at https://zenodo.org/records/13925651 (Zhang et al. 2024).

1 Introduction

The South China Sea (SCS) is a semi-enclosed marginal sea with a deep basin, making it the largest marginal sea in the tropics, covering approximately 3.5×10^6 km^2. The SCS is also the largest marginal sea in the western Pacific and is known for its powerful internal tides and abundant internal waves (Alford et al., 2015). Mesoscale eddies in the SCS transport heat and salt from the Kuroshio loop near the Luzon Strait (Yang et al., 2019) and modulate sea surface fields (Tan et al., 2023). The background circulations in the SCS are cyclonic in the upper and deep layers, whereas they are anticyclonic in the middle layer (Cai et al., 2020). The three factors contributing to the generally cyclonic gyre in the upper ocean of the northern SCS (Jilan, 2004; Liu et al., 2008) are (1) quasi-seasonal wind forcing, (2) net water transport into the SCS through the Luzon Strait, and (3) vorticity advection from the Kuroshio. The Kuroshio carrying the northwestern Pacific water intrudes into the SCS through the Luzon Strait (Nan et al., 2015).

Atmospheric forcing significantly influences the SCS, such as monsoons (Chen et al., 2023; Chen et al., 2022), tropical cyclones (TCs) (Guan et al., 2024; Shan et al., 2023), and the world's strongest boreal summer quasi-biweekly oscillation (Qi et al., 2023). Marine heat waves (Wang et al., 2022) and air–sea heat flux variations (Song et al., 2023; Zhang, 2023) are also observed in the northern SCS. This sector features broad continental shelves and steep continental slopes, leading to complex local ocean dynamical processes. For example, breaking internal tides on the continental slope induce along-slope deep sea bottom currents (Xie et al., 2018), and cross-isobathic motion of the water column or synoptic processes (e.g., TCs) induce continental shelf waves, such as topographic Rossby (Wang et al., 2019) and Kelvin mode (Li et al., 2024) waves.

Due to the complexity of air–sea interaction and oceanic processes in the SCS, local in situ observations are essential to uncovering their phenomena and mechanisms. From 2014 to 2015, a cross-shaped moored array comprising five buoys and four moorings was deployed in the northern SCS to acquire sea surface meteorological and upper and near-bottom oceanic data. This study lists the details of these observations and the resulting dataset. Some data have already been used in several studies focusing on air–sea heat flux, ocean temperature–salinity, and dynamical responses to TCs (Zhang et al., 2016; Zhang et al., 2018; Liu et al., 2020; Zhang, 2023) to investigate the effect of drag coefficients on surface heat flux during typhoons (Liu et al. 2022), the influence of typhoons on preexisting eddies (He et al., 2024), ocean mixing and heat flux by near-inertial waves (Hong et al. 2022; Lu et al., 2024), sea surface wind patterns (Zhang et al., 2020) and comparing microseism signals generated by typhoons (Lin et al., 2022), the validity of numerical model simulations (Wu et al., 2020; Lim Kam Sian et al., 2020; Lu et al., 2023), and deep ocean energy variability in the SCS (Quan et al., 2022). However, the full potential of this dataset has yet to be realized.

2 Moored array observations

2.1 Positions of buoys and moorings

The observation array comprised five buoys (B1–B5) and four moorings (M1, M2, M4, M5) in the northern SCS (Figs. 1 and 2), deployed from June to September 2014 and recovered from September 2014 to March 2015 (Table 1). The water depth at B1 and M1 was approximately 1600 m, whereas the depths at the other stations were greater than 3000 m. TCs significantly influenced the observations (Fig. 1), including Hagibis in June, Rammasun and Matmo in July, Kalmaegi and Fung-wong in September, and Hagupit in December. The information regarding these TCs was obtained from the China Meteorological Administration (https://tcdata.typhoon.org.cn/en/zjljsjj.html), which is more accurate for TCs affecting China (Lu et al., 2021; Ying et al., 2014). Although the designs of some buoys and moorings have been shown in previous studies (Zhang et al., 2016; Zhang, 2023), the designs of all the stations are redrawn to give more accurate information on the deployment of the instruments (Fig. 1b, Fig. 3).

Table 1 shows the locations of the observation stations and their time range. M1, M2, M4, and M5 were deployed during June 8–10, 2014, and successfully recovered during March 29–31, 2015 (Table 1). B1 was deployed on June 19, 2014, and maintained once on September 5, 2014. It lost contact on October 15 and was not recovered by two cruises from March 23 to April 4, 2015. B2 and B4 were deployed on July 29 and June 20, 2014, respectively, and recovered on March 30, 2015. B4 was maintained once on July 30, 2014. B3 was deployed on September 11, 2014. The tether of B3 snapped on September 15, 2014, when typhoon Kalmaegi passed over the observation array (Zhang et al., 2016). B3 then became a drifter, initially moving northeastward with circular tracks (Fig. 2a) attributed to the rightward advection and near-inertial surface currents induced by the typhoon. B3 returned to its initial location on September 21, 2014, moved eastward and turned back on September 25, 2014, and followed a southwestward track after that (Fig. 2a). A ship recovered B3 on October 17, 2014, and it was brought back to land on October 21, 2014. The moored part of B3 was recovered on March 31, 2015. B5 was deployed on August 26, 2014, and lost contact on October 11, 2014. The moored part of B5 was recovered on March 31, 2015. The horizontal movement of the buoys was minimal during observations because they primarily moved in a circular region with a radius shorter than 3 km (Figs. 2b–e). Typhoon Kalmaegi also increased the horizontal circular movement of B1 to approximately 4 km on the northwest side on September 15, which was attributed to the northwestward winds on the right-hand side of the typhoon, indicating that the typhoon moved the anchor of B1 northwestward because its tether length was approximately 2 km (nearly half of 4 km) (Figs. 2c and 3a).

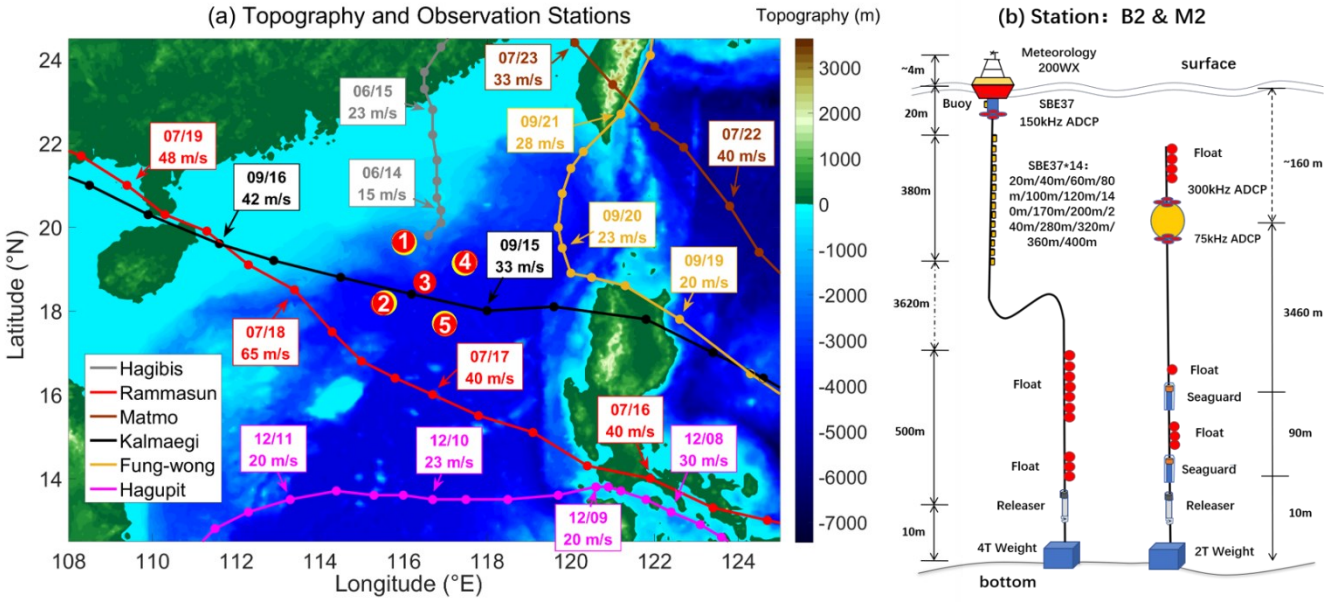

Figure 1. (a) Topography (m) map with the positions and deployed locations of the buoys (red dots) and moorings (yellow dots). **(b)** Designs of buoy 2 (B2) and mooring 2 (M2) are shown as examples; the dot-and-dash line indicates the tether length in the middle water of the buoy, and the dashed line indicates the depth of the two ADCPs on the top of the mooring. The tracks of the TCs are shown (colored lines) and their positions every 6 h (dots). The text boxes indicate the dates and the sustained maximum wind speed at UTC 00:00 on each date.

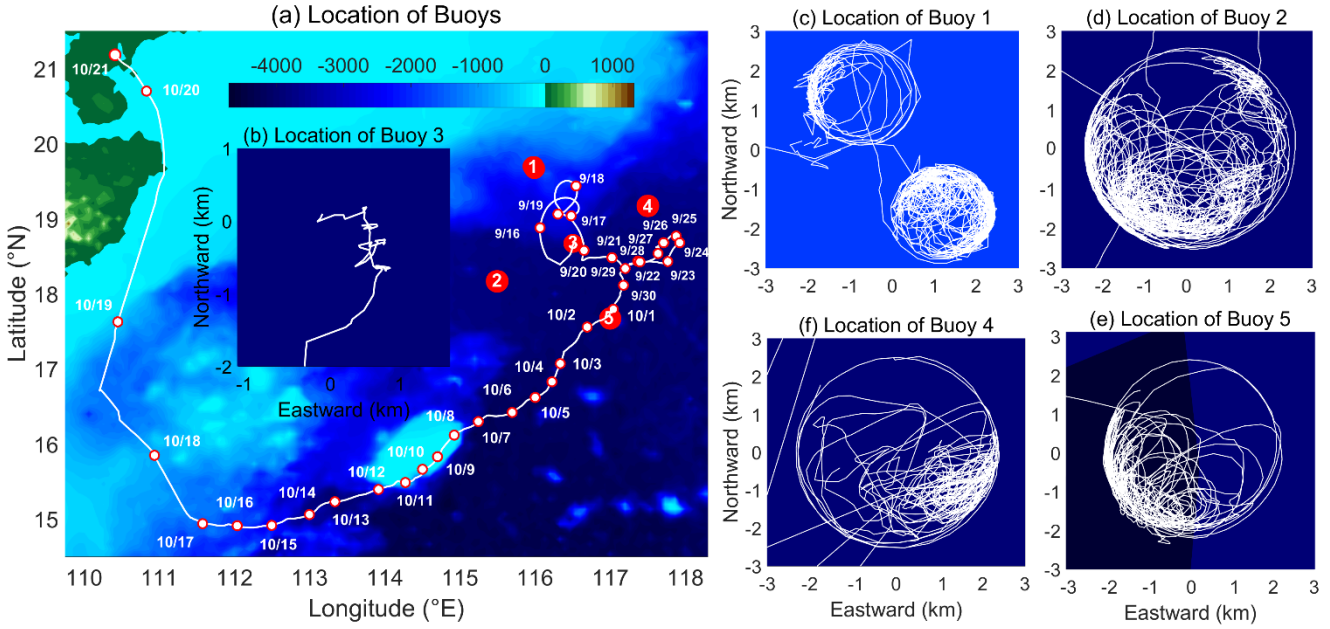

Figure 2. (a) Distributions of the buoy locations, with the track of buoy 3 (B3). **(b–e)** Tracks of buoys 3, 1, 2, 4, and 5 (B3, B1, B2, B4, and B5) with their locations relative to their initial deployed positions in northward and eastward directions (km). The white lines represent the buoy tracks, and the white hollow dots indicate the positions of B3 every day after September 15, 2014, when its tether snapped and it became a drifter.

Table 1. Information of the observation station

Station	Deployed Longitude (E)	Deployed Latitude (N)	Estimated Water Depth (m)	Time Range*
Buoy 1 (B1)	115°59’49.8”	19°40’04.8”	1625	2014.06.19–2014.10.15
Buoy 2 (B2)	115°29’53.5”	18°09’59.3”	3710	2014.07.29–2015.03.30
Buoy 3 (B3)	116°30’33.9”	18°40’40.2”	3310	2014.09.11–2014.10.17
Buoy 4 (B4)	117°30’11.4”	19°10’01.7”	3430	2014.06.20–2014.03.30
Buoy 5 (B5)	116°59’55.7”	17°39’58.8”	3930	2014.08.26–2015.03.31
Mooring 1 (M1)	116°01’17.1”	19°37’28.7”	1630	2014.06.08–2015.03.29
Mooring 2 (M2)	115°32’57.8”	18°11’29.5”	3740	2014.06.10–2015.03.30
Mooring 4 (M4)	117°27’16.8”	19°08’24.9”	3410	2014.06.09–2015.03.30
Mooring 5 (M5)	116°58’50.8”	17°42’18.1”	3930	2014.06.10–2015.03.31

*B1 was lost and not recovered, and the end time of B1 represents the latest time when observation data were received. Otherwise, the time range represents the deployment and recovery time for the stations.

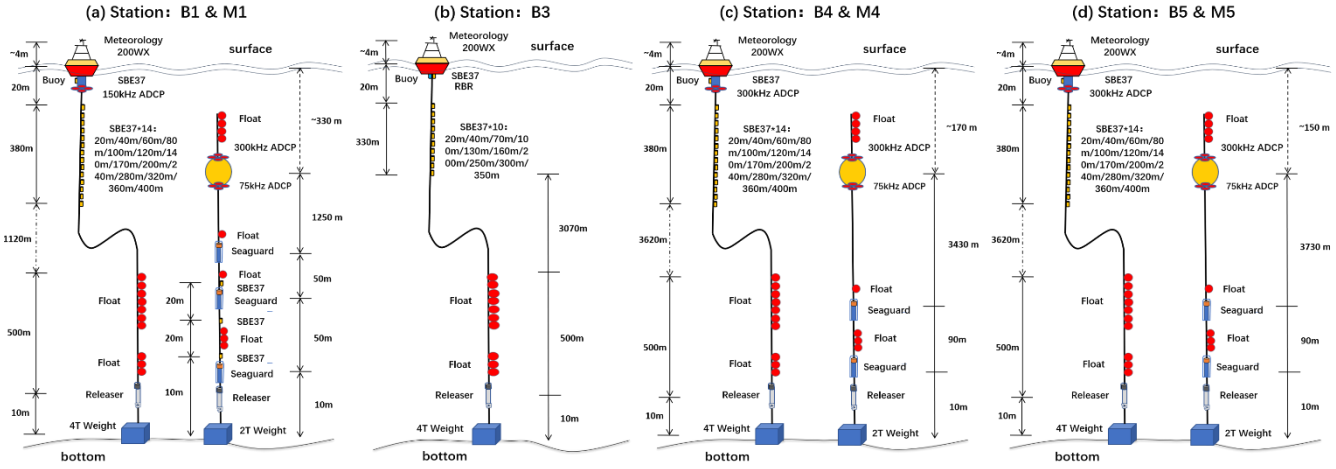

Figure 3. Design of stations 1, 3, 4, and 5. Note that all stations have a buoy and a mooring, except station 3, which only has a buoy. The dot-and-dash lines indicate the tether length in the middle water of the buoy, whereas the dashed lines indicate the depth of the two acoustic Doppler current profilers (ADCPs) on the top of the mooring.

Table 2. Observation data details at each station

	Stations	Recorded Data	Equipment and Position	Time Resolution
Buoy Location 1	B1–B5	Longitude (°E), Latitude (°N)	GPS sensor 1	1 h
Buoy Location 2			GPS sensor 2	
Buoy Location 3	B1, B2, B4, B5		GPS sensor 3	1 h (B1, B4), 3 h (B2) or 6 h (B5)
Meteorological data 1	B1–B5	Air temperature (°C), Air pressure (hPa), Relative humidity (%),	Meteorological sensors at 4 m height from sea surface	

Meteorological data 2		Compass (°), Wind speed (m/s, average and maximum), Wind direction (°, average and maximum), Rain guage (mm), Compass (°)	Auto meteorological station (200WX) at 4 m height from sea surface	12 min (B2) or 1 h (B1, B3, B4, B5)
Current 1*	B1, B2, B4, B5, M1, M2, M4, M5	Speed (cm/s), Direction (°), Vertical velocity (cm/s), Temperature, Bin (m), Real-time and designed depth of the ADCP (m, depth and depth0)	Downward-looking for ADCP 1, 3, and uplooking for ADCP 2	3 min (300 and 150 kHz ADCP) or 15 min (75 kHz ADCP)
Current 2	M1, M2, M4, M5	Speed (cm/s), Direction (°)	SeaGuard at 10 (M1, M2, M4, M5), 50 (M1) and 100 m (M1, M2, M4, M5) from ocean bottom	10 min
Sea temperature, salinity and pressure	B1, B2, B4, B5, M1	Temperature (°C), Salinity (psu), Pressure (dbar), Depth (m)	SBE-37 with design depth (m) at buoys: 20, 40, 60, 80, 100, 120, 140, 170, 200, 240, 280, 320, 360, 400 SBE-37 with design depth 10 and 50 m above the bottom at M1	2 min
Sea Surface Waves	B1, B4	Wave height (m, Significant and Maximum), Peak period (s), Mean wave direction (°), Wave spread	Wave gauge at sea surface (0 m)	1 h
Radiation (W/m^2)	B3	Short wave (upward, downward), Long wave (upward, downward), Air temperature (°C)	Wave radiometer at 4 m height from sea surface	1 h
Visibility (VIS, km)		Air visibility (km)	Visibility meter at 4 m height from sea surface	
Biochemistry data		Water pressure (dbar), Turbidity (V, two sensors), Chlorophyll (ug/L, Chla), Colored dissolved organic matter (ppb, CDOM)	RBR sensors at sea surface (0 m)	12 min

* Acoustic Doppler current profiler (ADCP) 1 was the downward-looking ADCP deployed at the buoy, ADCPs 2 and 3 were the upward and downward-looking ADCPs on the mooring, respectively. The 300 kHz ADCPs were binned in 4 m, with the first bin at 8 m (B4) or 6.24 m (M1, M2) and the last bin at 124 m (B4) or 122.24 m (M1, M2). The 150 kHz ADCPs were binned in 8 m, with the first bin at 14 m and the last bin at 246 m. The 75 kHz ADCPs were binned in 16 m intervals, with the first bin at 24.7 m and the last bin at 568.7 m. ADCP 1 at B5 was lost during observation and no data were recovered.

2.2 Dataset description

The dataset comprises 52 files in netcdf file (.nc) format containing air and ocean observation data and the positions of the buoys during 2014–2015, along with a metadata file in.txt format to briefly introduce the data. The observation instruments were calibrated before deployment. After output from the observation instruments, the observation data are transformed

directly to netcdf files, with the units and FillValues labeled. No special modification or quality control was applied to keep the original output data unchanged. All the files include Coordinated Universal Time (UTC) and local time, which is eight hours ahead of UTC (UTC +8) since 0000-01-01 00:00:00. The local time is also called China Standard Time or Beijing Time. The location data are longitude (°E) and latitude (°N), observed by Global Positioning System (GPS) sensors. B1, B2, B4, and B5 had three GPS sensors, and B3 had two. Location-1 data were obtained from the primary GPS sensors on the body of the buoys, Location-2 data were obtained from the GPS sensors approximately 4 m above the sea surface, and Location-3 data were obtained from the low-frequency GPS sensors at the bottom of the buoys (approximately 0 m). The measurement accuracies of the GPSs were <50 m.

The air data include observations approximately 4 m above the sea surface from meteorological sensors (meteorology data) and the automatic meteorological station (200WX data). Two meteorological stations are deployed on the buoys to provide a backup if the sensors of a meteorological station break down during observation. The 200WX data are similar to the meteorology data but exclude rain gauge data. The wind direction indicates the direction of the incoming wind; for example, 0° indicates wind passing from north to south, and 90° indicates wind passing from east to west. The compass indicates the direction of the meteorological sensors or stations, referring to the attitude of the sensors or stations. For the measurement accuracies of 200WX, the air pressure is ±1 hPa, the air temperature accuracy is ±1.1 °C, the relative humidity is ±5%, the compass is 1° for static heading and 2° for dynamic heading, and the measurement accuracy of wind differs in dry and wet conditions. In dry conditions, the wind speed accuracy is 0.5 m/s + 10% of reading for low winds (0–5 m/s), or a greater value of 1 m/s or 10% for high winds (5–40 m/s), the wind direction accuracy is 5° for low winds (2–5 m/s) and 2° for high winds (>5 m/s). In wet conditions, the wind speed accuracy is 2.5 m/s and 8°. The measurement accuracy of the meteorological sensors is in the same order as 200WX. For the meteorology data of B3, there was a visibility meter to measure air visibility (km), a Campbell Scientific NR01 four-component net radiometer approximately 4 m above the sea surface with outputs every 1 h, measured upward and downward shortwave and longwave radiation (W/m^2), and air temperature observed by the radiometer (°C). The measurement accuracy is ±10% of the measurement range for air visibility, <2.4% for shortwave radiation, and <7% for longwave radiation.

The ocean data includes sea surface waves observed by a TRIAXYS^{TM} OEM wave recorder (Wave data), the temperature, salinity, and pressure using conductivity, temperature, and depth (CTD) recorders observed by Sea-Bird Scientific 37 recorders (SBE data), currents observed by Teledyne RD Instruments (TRDI) acoustic Doppler current profilers (ADCP data), and currents observed by Aanderaa Data Instruments SeaGuard Recording Current Meter (SeaGuard data), as well as Biochemistry data observed by multi-parameter Richard Brancker Research (RBR) sensors (RBR data). The 75 kHz ADCP was a TRDI Workhorse Long Ranger, the 150 kHz ADCP was a TRDI Workhorse Quartermaster, and the 300 kHz ADCP was a TRDI Workhorse Sentinel. Sea surface wave data includes significant wave height (m), maximum wave height (m), mean wave direction (°), peak period (s), and wave spread (Table 2). The observation accuracy is better than 2% of the measurement range for pressure for wave height and period and ±1° for wave direction. Wave recorders were deployed on B1, B4, and B5, but the

wave recorder on B5 broke down, resulting in low-quality data. Consequently, only sea surface wave data from B1 and B4 were included in the ocean data.

SBE data include temperature (°C), salinity (psu), and pressure (dbar) observed by SBE-37 CTD sensors. The measurement accuracies of SBE-37 are ±0.002 °C (−5 to 35 °C) or ±0.01 °C (35–45 °C) for temperature, ±0.0003 S/m for electrical conductivity, and 1% for pressure. Serial 1–15 in the SBE data refer to the SBE-37 sensors from the surface to the ocean bottom. All SBE sensors are deployed on the buoys, except for three SBE-37s on the moorings near the ocean bottom (Figs. 1b and 2). The SBE-37 strings on B1 and B3 were lost during deployment; therefore, only SBE data at the sea surface at the bottom of the buoy (Temperature1, Salinity1, and Pressure1) were obtained. Two SBEs on B4 broke down during observation, resulting in data from only 13 SBEs. The ADCP data comprise current speed (cm/s), current direction (°), temperature observed by ADCP (°C), depth of the ADCP (m), designed depth (depth0), and bin intervals of the ADCP observation (m). The SeaGuard data include current speed (cm/s) and direction (°). Unlike wind direction, current direction indicates the direction of the current flow; for example, 0° indicates the current passing from south to north, and 90° indicates the current passing from west to east. In SeaGuard data, the accuracy is ±1° of reading for current speed and ±3° (if the tilt is 0–15°) or ±5° (if the tilt is 15–35°) for the current direction.

Negative bin values refer to downward-looking ADCPs and vice versa. ADCPs on the buoys (ADCP 1) were downward-looking, located at the sea surface (approximately 0 m); their observation range was depth0 + bin. The ADCP data on the moorings comprise upward-looking (ADCP 2) and downward-looking (ADCP 3) observations with ranges depth + Bin because the depth of the ADCPs at the moorings varies during observation. B3 did not have ADCP or SeaGuard observations (Fig. 3 and Table 2), and the ADCP at B5 broke down, and no data were obtained. For the bin sizes of the ADCPs, the 300 kHz ADCPs were binned in 4 m, with the first bin at 8 m (B4) or 6.24 m (M1 and M2) and the last bin at 124 m (B4) or 122.24 m (M1 and M2). The 150 kHz ADCPs were binned in 8 m, with the first bin at 14 m and the last bin at 246 m. The 75 kHz ADCPs were binned in 16 m intervals, with the first bin at 24.7 m and the last bin at 568.7 m. The velocity accuracy for the 75 kHz ADCPs is 1% of water velocity relative to the ADCP ±0.01 m/s (written as 1% ± 0.01 m/s). The accuracies for the 150 and 300 kHz ADCPs are 1% ± 0.005 m/s and 0.5% ± 0.005 m/s, respectively. The RBR sensors were only deployed at B3 and observed water pressure (dbar), turbidity (V) by two sensors, chlorophyll (ug/L Chla), and colored dissolved organic matter (CDOM; ppb). The measurement accuracy of water pressure was ±0.05%, ±2% for turbidity and chlorophyll, and ±0.01 ppb for CDOM.

3 Results

The data at station 2 (B2 and M2) were longer and more complete than those at the other stations and are shown first to provide an example of the observations at the stations. Subsequently, observations differing from station 2 are also shown, including near-bottom observations at B1, sea surface waves at B1 and B4, and the observations at B3 after its rope snapped on September 15, causing it to become a drift.

3.1 Sea surface air and ocean observation at station 2

The prevailing wind direction was approximately 200° (nearly south wind) from late July to mid-August, then shifted primarily in the range of 20°–80° (nearly northeast wind) after October, with wind direction variations during September (Fig. 4b, d). This finding indicates that the transition occurred from local summer to winter monsoon, with September as the transition month. The average wind speed was less than 10 m/s during July and August, often exceeding 10 m/s after October (Fig. 4a, c), indicating that the winter monsoon was stronger than the summer monsoon at B2. B2 likely traveled through the eye of typhoon Kalmaegi, with two wind speed peaks accompanied by minimum air pressure (Zhang et al., 2016). Typhoon Kalmaegi and severe tropical storm Fung-wong during September significantly influenced the wind direction at B2, with the wind direction turning counterclockwise near September 15 and 21, consistent with B2 being on the left side of both TCs.

B2 also recorded a drop in sea surface air and ocean temperature (Fig. 4g, i) from summer to winter, ranging from approximately 28.5 °C to 30.5 °C in August, decreasing from approximately 29 °C to 27 °C in October, and continuing to decrease further. The surface air temperature was slightly lower than the sea surface temperature during the observation period, indicating local sensible heat flux from the ocean to the atmosphere because the water cooled slower than air during fall. Due to their high time resolution (2 min), the observations also captured the diurnal temperature variation attributed to daytime solar radiation heating, nighttime outward longwave radiation cooling, and the deepening of the ocean mixed layer. Typhoon Kalmaegi and tropical storm Fung-wong successively decreased the sea surface air and ocean temperatures during September, with Kalmaegi suddenly decreasing the sea surface temperature by approximately 2.5 °C because B2 was located in the core cooling area on the right-hand side of the typhoon track.

Rain gauge data were measured using a tipping bucket rain gauge, with a maximum measurement of 255 mm. The bucket empties when full (255 mm), and the measurement starts from 0 mm again. The rain rate can be calculated by dividing the difference in rain gauge values by the time interval. Significant rainfall events were recorded around August 2, September 6, 15, and 21. Typhoon Kalmaegi and severe tropical storm Fung-wong induced strong rainfall around September 15 and 21. Evaporation also affected rain gauge values, which decreased slowly over time without precipitation, indicating that rain gauge data reflected precipitation and evaporation. Sea surface salinity increased from approximately 33.3 psu near October 1 to approximately 33.8 psu near November 10 (Fig. 4i) due to little rainfall, with salinity primarily controlled by evaporation.

Some similarities and differences existed between the two meteorological observations: the European Centre for Medium-range Weather Forecasts (ECMWF) Reanalysis v5 data (ERA5, https://www.ecmwf.int/en/forecasts/dataset/ecmwf-reanalysis-v5) are used to evaluate their performance. The average and maximum wind speed and direction in the meteorology and 200WX datasets are consistent, and the average wind matched the wind speed from ERA5 well, except that the average wind direction observed by meteorological sensors suddenly turned to approximately 180°, and the maximum wind direction varied rapidly between 0° and 360° after November 15 (Fig. 4b, d), indicating some malfunctions of the wind meteorological observation sensor. Air pressure measurements from the meteorological sensors, 200WX station, and ERA5 are consistent before August 27, with the diurnal air pressure variation observed by the meteorological sensors amplifying and becoming

inconsistent with the 200WX observations and ERA5 after August 27 (Fig. 4f), indicating some malfunction of the pressure meteorological observation sensor. The sensitivity of the air temperature measurements by the 200WX was greater than that of the temperature meteorological sensor, with larger amplitude diurnal variations, whereas their values were a bit greater or different from ERA5 data (Fig. 4g). Relative humidity measured by the meteorological sensor was consistent with ERA5 data and was greater than that measured by the 200WX, ranging from 0% to 10% (Fig. 4h). Both meteorological observations showed missing data approximately 5 days near October 6, which might be due to the malfunction of the instruments or data recording.

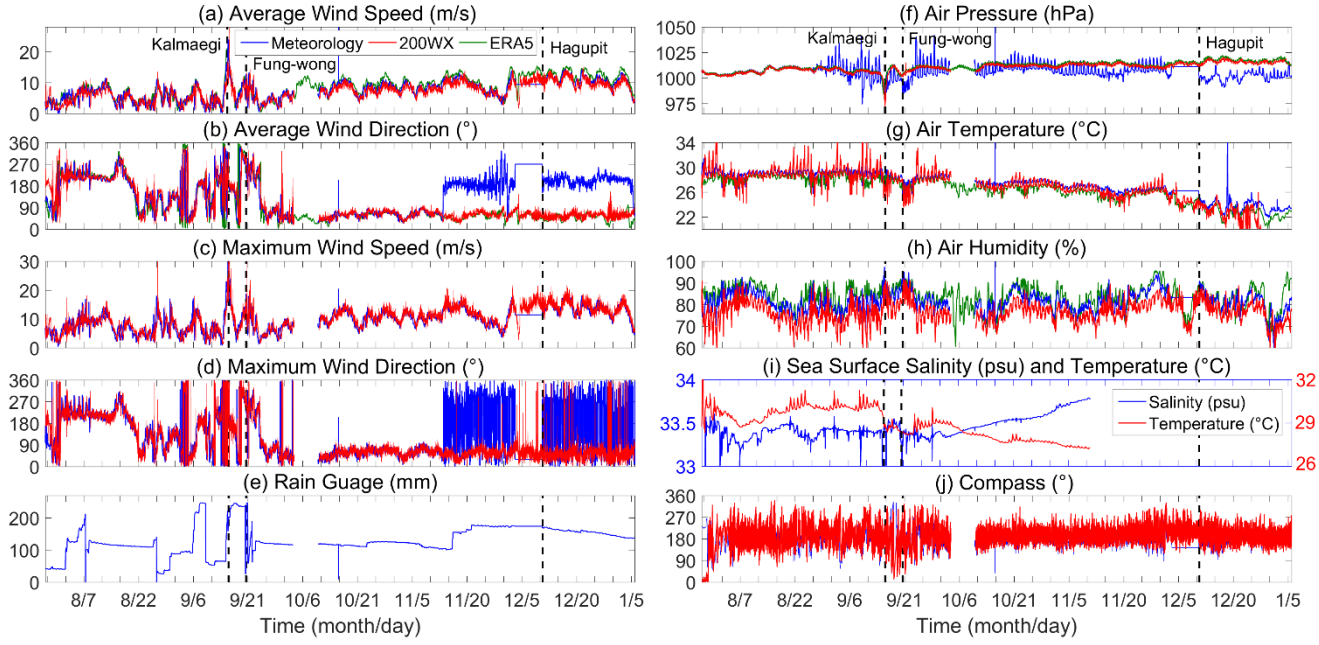

Figure 4. Observation at Buoy 2 (B2): the average and maximum wind speeds (**a**, **b**; m/s) and direction (**c**, **d**; °), rain gauge (**e**; mm), air pressure (**f**; hPa), air temperature (**g**; °C), relative humidity (**h**; %), sea surface salinity (**i**; psu), sea surface temperature (**i**; °C), and buoy compass (**j**; °). The blue and red lines are data observed by the meteorological sensors and the 200WX automatic meteorological station, approximately 4 m above the sea surface. The blue and red lines in (**i**) represent salinity and temperature observed by the SBE-37 sensor at the buoy bottom (approximately 0 m). The wind directions indicate the direction from which the wind originates. The vertical dashed lines indicate the time when TCs Kalmaegi, Fung-wong, and Hagupit were closest to B2. The green lines are the European Centre for Medium-range Weather Forecasts (ECMWF) Reanalysis v5 (ERA5) data.

3.2 Current, temperature, and salinity observation at station 2

At station 2, the current observations at the mooring (Figs. 5b–d) were longer than those at the buoy (Fig. 5a), and the temperature and salinity (Fig. 6) observations at the buoy due to the deployment and recovery times. The upward-looking 300 kHz ADCP (Fig. 5b) and the SBE-37 recorder at the bottom of the buoy (Fig. 6) stopped working near November 11 while the data quality from the downward-looking 75 kHz ADCP at the mooring decreased, especially in 2015, with some missing data at several bins (Fig. 5b). Although the SBE chain was 400 m long, the observation range of temperature and salinity was primarily shorter than 400 m because the rope swung and tilted during observations, especially the deepest observation depth

decreased to ~200 m near September 21 under the influence of typhoon-induced near-inertial waves after Kalmaegi. Similarly, the positions of the ADCPs at the moorings also moved vertically due to the tilt of the mooring rope, especially when influenced by intensified currents after Rammasun and Matmo in July and Kalmaegi in September.

ADCPs and SeaGuards captured horizontal currents induced by diurnal and semi-diurnal tides as well as vertical variations in temperature and salinity isolines. The upper ocean background current speed was primarily <20 cm/s, significantly increasing after TCs Rammasun and Matmo in July, Kalmaegi in September, and Hagupit in December, with the mixed layer current speed reaching approximately 150 cm/s after Kalmaegi (Zhang et al., 2016). Typhoon Kalmaegi immediately strengthened the near-inertial mixed layer currents and kinetic energy, which then propagated horizontally and vertically with the dispersion of near-inertial waves and regulation by background vorticity (Lu et al., 2023; Lu et al., 2024; Zhang et al., 2016). Near-bottom currents were primarily <10 cm/s and near-bottom flow turned from northeastward to southeastward after the influence of typhoon Rammasun.

The upper ocean temperature decreased monotonously from the surface (approximately 0 m) to approximately 400 m, and salinity exhibited a low–high–low vertical structure with a maximum of approximately 34.5 psu from approximately 100 m to 250 m. There is long-term upper ocean cooling and a decrease in salinity from summer to winter (Fig. 6), especially after mid-October. Kalmaegi reduced the sea surface temperature by approximately 1.9 °C at its maximum, with a subsurface cold anomaly of approximately 1.1 °C (Zhang et al., 2016) due to its proximity to the typhoon track, where typhoon-induced mixing and upwelling primarily modulated the upper ocean temperature (Zhang, 2023; Zhang et al., 2018). Vertical variations in temperature and salinity were also influenced by eddies, fronts, and flows (Liu et al., 2017; Lu et al., 2024), but these are not pursued further here. The downward propagation of warm or freshwater anomalies from the surface and the diurnal cycle of the near-surface mixed layer can also be observed (Fig. 6) and partly analyzed in Zhang (2023).

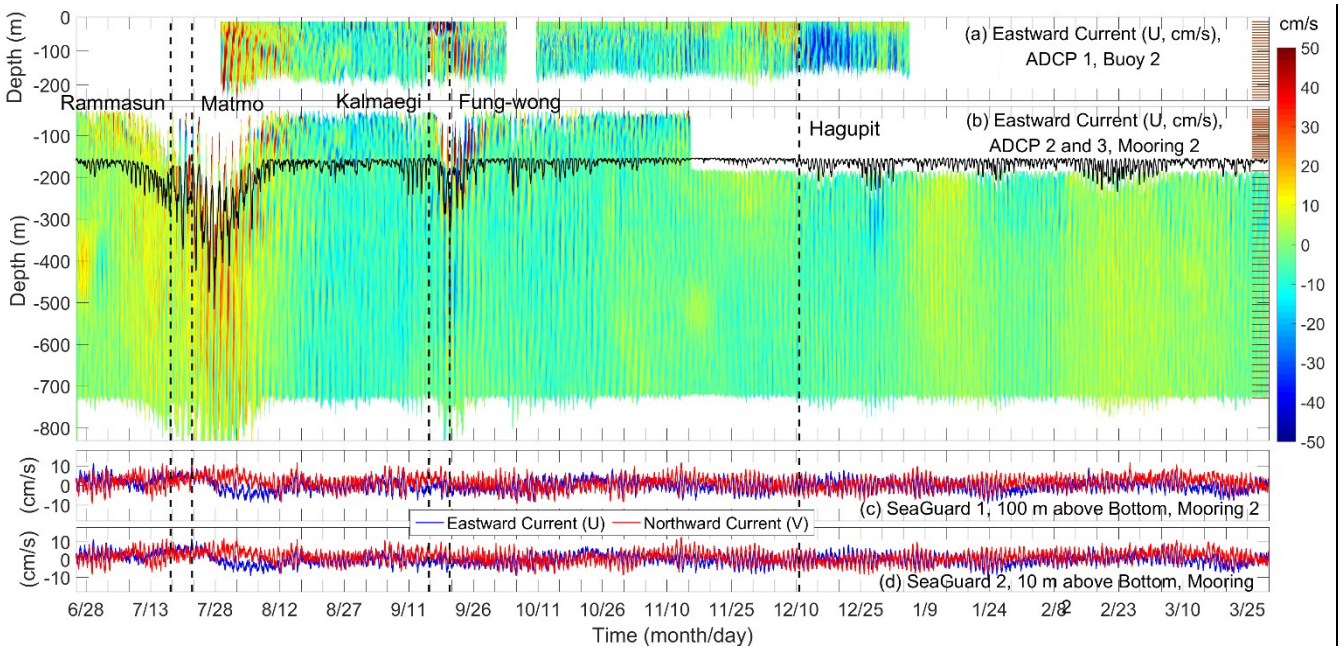

Figure 5. (a–b) Eastward currents (m/s) observed by the downward-looking 150 kHz ADCP at the buoy bottom **(a)** and the combination of the upward-looking 300 kHz and downward-looking 75 kHz ADCPs at the mooring **(b)**. **(c, d)** Eastward (U) and northward (V) currents are observed by the SeaGuard current meter at 100 m **(c)** and 10 m **(d)** above the ocean bottom. The black solid line in **(b)** represents the vertical positions of ADCPs 2 and 3. The vertical dashed lines represent the time when the TCs are closest to Buoy 2. The brown lines in **(a)** and **(b)** represent the initial depth of the observation bins of the ADCPs.

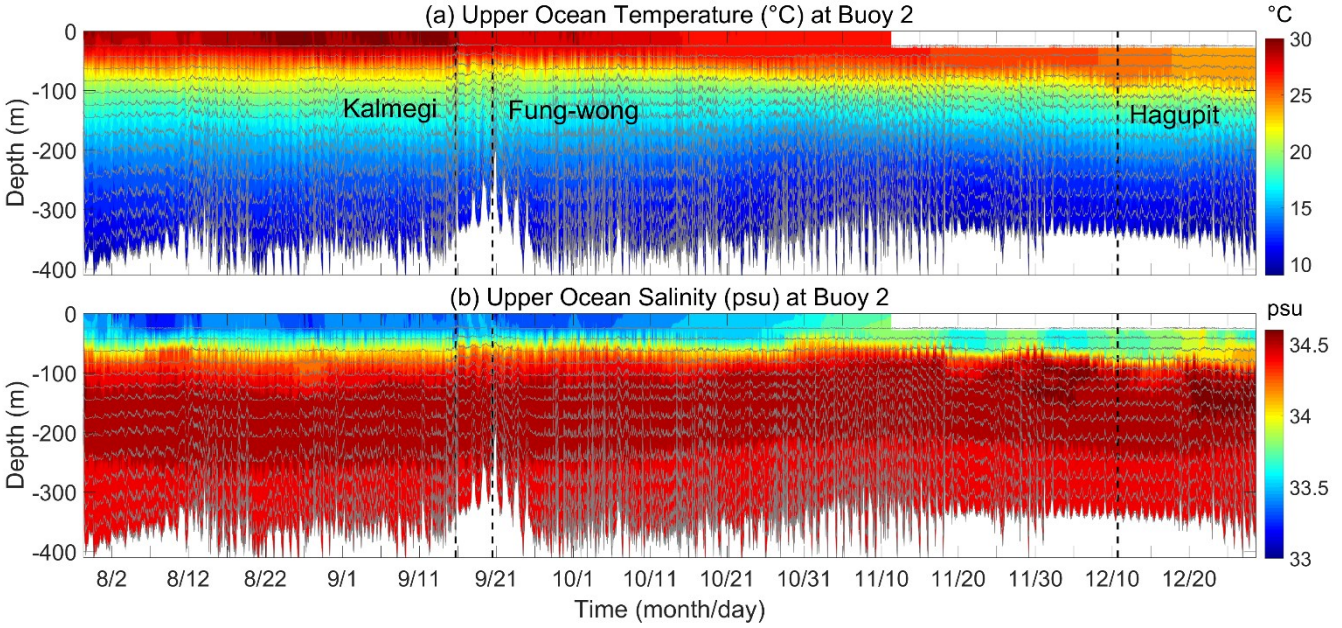

Figure 6. Upper ocean temperature (**a**; °C) and salinity (**b**; psu) observed by the chain of SBE-37 sensors at buoy 2. The vertical dashed lines indicate the time when the TCs are closest to Buoy 2. The gray lines represent the time variation of the depth of the SBE-37 sensors.

3.3 Near-bottom observation at mooring 1

The instruments at M1 differed from those at other moorings; their observations are analyzed and discussed here. Three SBEs were deployed near the ocean bottom to evaluate the homogeneity of the near-bottom layer. The variation in near-bottom pressure observed by the three SBEs at approximately 10, 30, and 50 m above the ocean bottom is tiny (Fig. 7a), indicating minimal swing and tilt of the rope near the bottom of M1. The water pressure at approximately 10 m above the bottom was approximately 1710 dbar, corresponding to a depth of approximately 1690 m, indicating that the water depth of M1 was approximately 1700 m. The temperature varied from 2.5 °C to 2.7 °C, and salinity was close to 34.6 psu at the three SBEs (Fig. 7b, c). The temperature, salinity, and currents observed from the three SBEs and SeaGuards were close, indicating a uniform near-bottom layer greater than 100 m (Fig. 7d). However, the current at 100 m above the bottom differed from the other two layers during July 19 to August 12 and December 13 to 20, when the near-bottom flow also turned at M1, possibly influenced by super typhoons Rammasun and Hagupit (Fig. 7e).

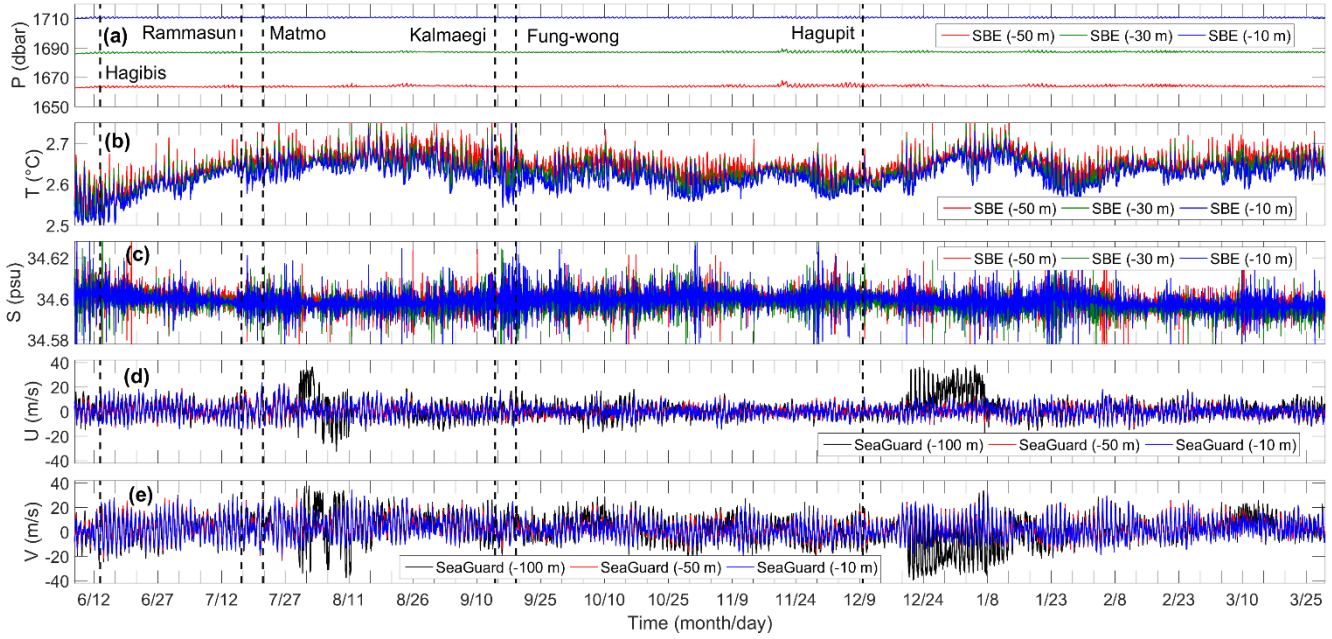

Figure 7. (a–c) Pressure (dbar; **a**), temperature (°C; **b**), and salinity (psu; **c**) observed by the SBE-37s at the mooring at approximately 50 (red), 30 (green), and 10 m (blue) above the ocean bottom. **(d–e)** Eastward current (cm/s) and northward current observed by the SeaGuard current meter at the mooring at approximately 100 (black), 50 (red), and 10 m (blue) above the ocean bottom. The vertical dashed lines represent the time when the TCs were the closest to Mooring 1.

3.4 Sea surface waves

Sea surface waves observed at B1 and B4 also merit further explanation. The variations in sea surface waves from the two wave gauges at B1 and B4 are similar (Fig. 8), indicating that the characteristics of the sea surface waves at the observation array were comparable. However, B4 showed more drastic variation in the peak period than B1, with different mean wave

directions and wave spreads from July 14 to 20 and near July 26, indicating the influence of TCs Habibis and Matmo. The observations at B1 were longer than at B4 but with some missing recordings from August 1 to August 17.

Sea surface winds, e.g., monsoon and TCs, primarily controlled the sea surface waves. During the summer monsoon (before September), the significant wave height was primarily <2 m, maximum wave height <3 m, peak period <10 s, and the mean wave direction was close to 180° (northward). During the winter monsoon (after October), significant and maximum wave heights increased to >3 m and >5 m, respectively, and the peak period to >10 s and the mean wave direction nearly 90° (westward). The wave spread ranged from 20 to 80 throughout the observation period of the two wave gauges (Fig. 8e). The TCs strongly influenced the local sea surface waves. Significant wave height increased to approximately 5, 10, and 3 m (Fig. 8a), whereas maximum wave height reached approximately 8, 15–18, and 5–6 m (Fig. 8b) owing to the influence of TCs Rammasun, Kalmaegi, and Fung-wong, respectively. The sea surface wave height increased rapidly in one day, along with a clockwise rotation of the mean wave direction and an increase in the peak period, then returned to background conditions within approximately three days, with the mean wave direction rotating counterclockwise and a decrease in the peak period (Fig. 8).

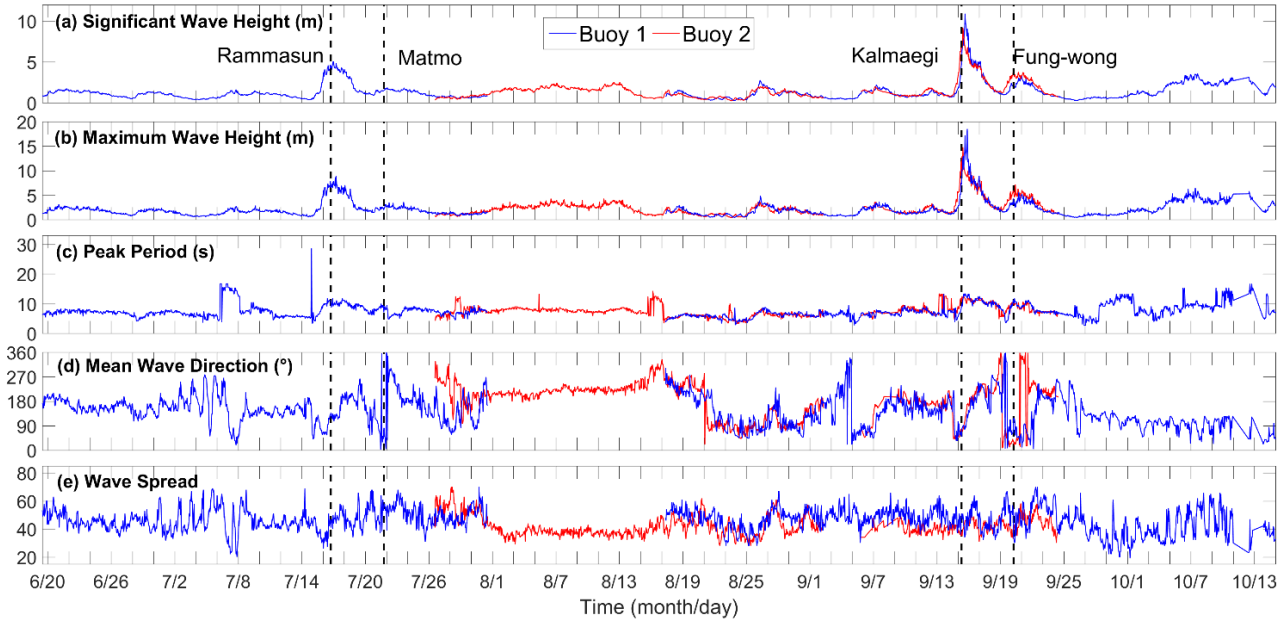

Figure 8. Significant wave height (**a**; m), maximum wave height (**b**; m), peak period (**c**; s), mean wave direction (**d**; °), and wave spread observed by the wave recorders at the bottom of buoys 1 (blue) and 4 (red). The vertical dashed lines represent the time when the TCs were the closest to the moored array.

3.5 Observation at buoy 3

Since the tether of B3 snapped on September 15, causing the buoy to become adrift (Fig. 2), it is crucial to describe B3 observations in this section, which partly reflects the air–sea conditions in region B3 (Figs. 9 and 10).

The average and maximum wind speeds increased to approximately 20 and 25 m/s, respectively, during Kalmaegi, with the wind direction changing rapidly (Fig. 9a). The average and maximum wind speeds reached approximately 10 m/s during Fung-wong, with the wind direction rotating counterclockwise because B3 was on the left side of the TC track (Fig. 9b). In October, the wind direction was primarily close to 0°, consistent with B2 (Fig. 4), indicating that the monsoon controlled the local region from nearly north to south. The rainfall was strong during Kalmaegi (approximately 250 mm) and Fung-wong (approximately 200 mm), accompanied by low air pressure (980 and 1000 hPa). However, there was little rainfall, and the air pressure increased to more than 1100 hPa after September 24 (Figs. 9e, f). The diurnal air pressure variation can also be found in the observation. The sea surface temperature continuously decreased from ~30 °C to ~27.5 °C and ~26.5 °C after Kalmaegi and Fung-wong, respectively, and then recovered back to ~29 °C in October (Fig. 10d). Note that the surface air temperature (Fig. 9g) was 1–3 °C colder than the sea surface temperature (Fig. 10d) during the observation, indicating sensible heat flux from the ocean to the air in Autumn along the track of B3. The relative humidity was 85% to 100% during Kalmaegi and Fung-wong (September 14–25) and then continuously decreased to approximately 70% in October (Fig. 9h), consistent with the fact that the TC-induced cold wake results in reduced rainfall and sea surface humidity (Ma et al., 2020). Air visibility was approximately 10 km when B3 was deployed, then decreased to approximately 1 m due to cloud cover and adverse sea surface conditions from typhoon Kalmaegi, and rapidly increased to approximately 16 km on September 15 due to the passage of the typhoon eye (Fig. 9i). Clear sky returned near September 17 while subsequent tropical cyclone Fung-wong increased air visibility at B3 to approximately 16 km again on September 20, lasting until September 22–23.

B3 was the only buoy equipped with a radiometer. The maximum shortwave radiation observed by the upward sensor was approximately 1900 W/m^2 near noon (Fig. 10a) when solar radiation was the strongest, significantly reduced by cloud cover from the TCs from September 13 to 23 and moderately reduced by local cloud cover in October. Conversely, the shortwave radiation observed by the downward sensor was much (one order) smaller than the upward shortwave radiation, indicating a minimal reflection of solar radiation. Similarly, the longwave radiation observed by the upward and downward sensors was close to 0 W/m^2 and approximately −50 W/m^2 (Fig. 10b), respectively, indicating that longwave radiation was primarily from the ocean to the atmosphere, with minimal contribution from the atmosphere to the ocean. The sea surface temperature (Fig. 10(d)) decreased from approximately 30 °C to 27 °C after Kalmaegi, recovering to approximately 29 °C in October. The air temperature observed by the radiometer (Fig. 10c) followed a similar variation pattern to that observed by the meteorological sensors (Fig. 9a) and sea surface temperature (Fig. 10d), with significant diurnal variation. The sea surface salinity (Fig. 10d) increased from approximately 33.5 psu to 33.7 psu due to typhoon Kalmaegi, despite strong rainfall (Fig. 9e). The variation in sea surface salinity was consistent with the rain gauge data, except for a decrease from October 3 to 5.

Some recording errors of sea surface temperature and salinity occurred after October 5 (Fig. 10d, e), with a sudden change in the values. The SBE and RBR sensors were deployed at 1.3–1.6 m from the surface, with pressures of 1.3 hPa–1.6 hPa (Fig. 10f). Chlorophyll observed by the RBR sensor (Fig. 10g) showed diurnal variation, increasing from approximately 2 ug/L to 2.5 ug/L after Kalmaegi and Fung-wong, then returning to approximately 2 ug/L. Turbidity observed by the first sensor (Fig. 10h) is more than 0.05 V before September 15. It then decreased to approximately 0.005 V, making it challenging

to determine whether the decrease was attributable to Kalmaegi, which made the sea surface cleaner, or to damage to the turbidity sensor after B3's rope snapped. Conversely, turbidity observed by the second sensor (Fig. 10i) remained near 4.4569 throughout the observation period of B3 (Fig. 10i). CDOM (Fig. 10j) gradually increased from 1.88 ppb in September to 2.1 ppb by mid-October.

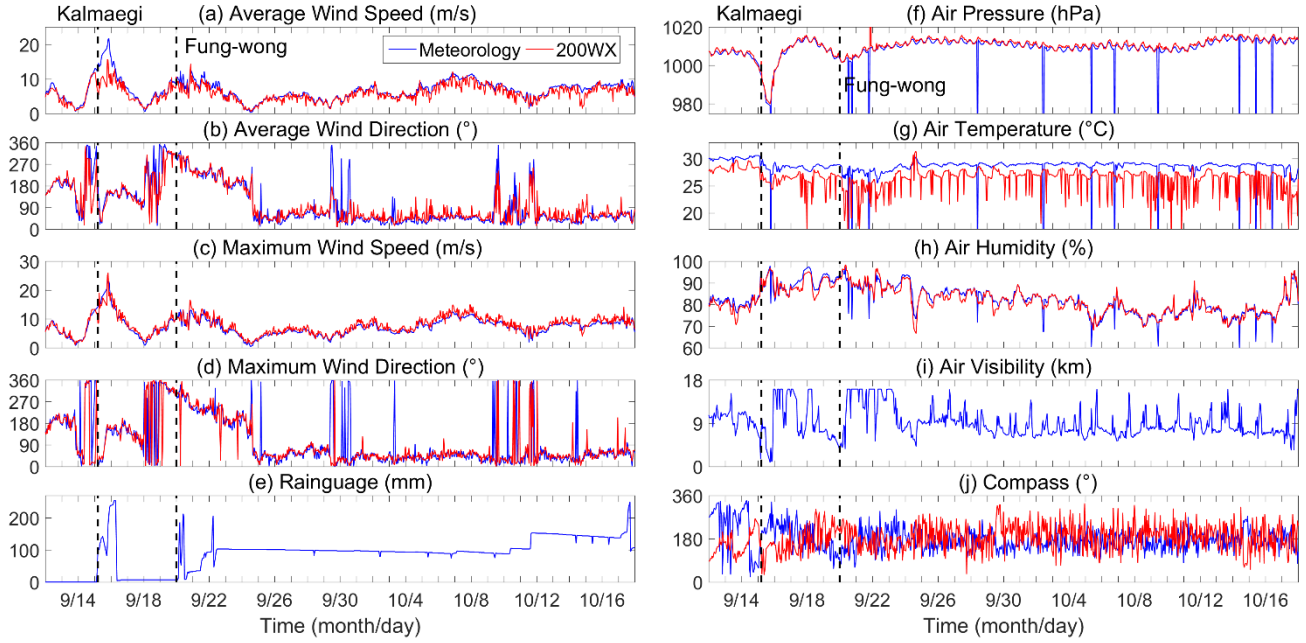

Figure 9. Similar to Figure 4 but for buoy 4. Notably, **(i)** is the air visibility (km) observed by a visibility meter 4 m above the sea surface. The vertical dashed lines represent the time when the TCs were the closest to the moored array.

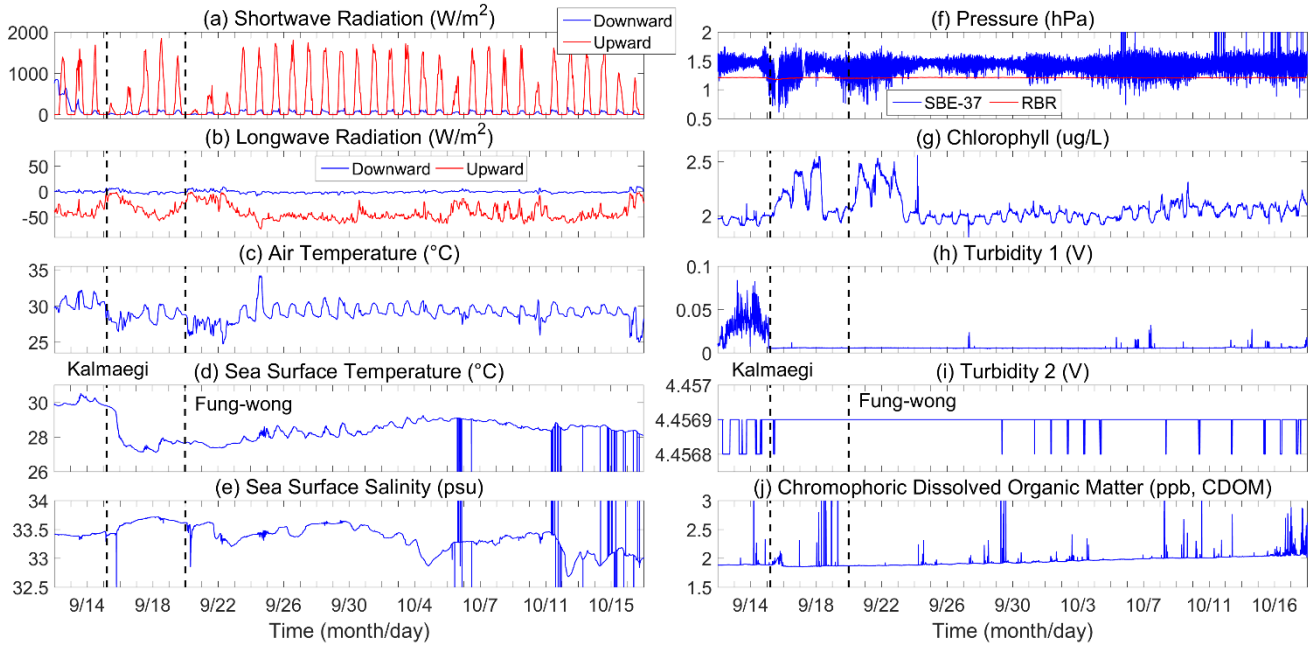

Figure 10. Observation at Buoy 3. (a–c) Shortwave radiation (a; W/m^2) and longwave radiation (b; W/m^2) observed by upward (red) and downward (blue) radiation sensors and the air temperature observed by the radiometer (c; °C). (d–f) Sea surface temperature (f; °C), salinity (g; psu), and pressure (h; hPa, blue) observed by SBE-37, with pressure (h; hPa; red) observed by RBR sensors. (g–j) Chlorophyll (g; ug/L), turbidity observed by two sensors (g–h; V), and chromophoric dissolved organic matter (DCOM; j; ppb). The radiometer is 4 m above the sea surface, and the SBE-37 and RBR sensors are at the bottom of buoy 3 (approximately 0 m). The vertical dashed lines represent the time when the TCs were the closest to the moored array.

4. Data availability

All data are publicly available through the Zenodo repository at https://zenodo.org/records/13925651 (Zhang et al., 2024). The data will also be publicly available on the website of the Southern Marine Science and Engineering Guangdong Laboratory (Zhuhai) (http://www.hellosea.org.cn/#/metadataDetail/en-US?detailId=8f32902492b84dc1a80f0f717a7c827e) when the manuscript is published. This study provides a detailed dataset description, including a time series of sea surface meteorological elements, sea surface waves, ocean temperature, salinity, and currents collected from a moored array comprising five buoys and four moorings during 2014–2015. The meteorological elements include wind, temperature, pressure, rain gauge, and humidity data. Furthermore, data from the buoy at the center (B3) include sea surface visibility, radiation (shortwave and longwave), and biochemistry observations (chlorophyll, turbidity, and CDOM).

5 Conclusions

This study presents an observation dataset from a cross-shaped moored array comprising five buoys (B1–B5) and four moorings (M1, M2, M4, M5) with synchronous atmospheric and oceanic data in the northern SCS during 2014–2015 (MASCS

1.0). The atmospheric data are observed by two meteorological instruments at the buoys. The atmospheric data are observed by two meteorological instruments at the buoys. The oceanic data consist of sea surface waves recorded by a wave recorder and temperature and salinity from the surface to a depth of 400 m and at 10 and 50 m above the ocean bottom using CTD recorders. It also includes currents from the surface to a depth of 850 m measured by ADCPs and at 10, 50, and 100 m above the floor measured by current meters. Additional measurements were taken for sea surface radiation, air visibility, chlorophyll, turbidity, and CDOM at B3, which was at the center of the moored array. The whole moored array was deployed in June 2014 and totally recovered at the end of 2015. Although some instruments and buoys broke down or were lost during observation, resulting in no data recovery or deficiencies, this dataset is valuable for further studies to uncover air–sea interactions and oceanic processes in the northern SCS.

For example, TCs Hagibis in June, Rammasun and Matmo in July, Kalmaegi and Fung-wong in September, and Hagupit in December 2014 traveled over the SCS and influenced the time series of the observations. The TCs increased the sea surface wind speed, enhanced the sea surface wave height and near-surface ocean currents, cooled the sea surface water and air temperature, also induced near-inertial waves and near-bottom currents. The moored array also transitioned from the summer to winter monsoons, with prevailing nearly south wind (approximately 200°) and waves (approximately 180°) with a sea surface significant wave height of <2 m and a peak period of <10 s from late July to mid-August. It then shifted to a nearly northeast wind (approximately 20°–80°) and east waves (approximately 90°), with a sea surface significant wave height of >3 m and a peak period of <10 s after October. Furthermore, ocean data might have recorded multiscale air–sea interactions and ocean processes, such as air–sea heat and momentum fluxes, ocean tides, internal waves, seasonal variations in temperature, salinity, and flows, and background processes, such as mesoscale eddies and local circulations.

The data have been used for analyzing the air–sea and ocean variations on the moored array (Quan et al., 2022; He et al., 2024), validating ocean (Zhang et al., 2016; Liu et al., 2020; Lu et al., 2023) and air–sea coupled (Wu et al., 2020; Lim Kam Sian et al., 2020; Liu et al., 2024) model simulation, evaluating the parameterization of air–sea surface flux (Zhang et al., 2020; Liu et al., 2024), and investigating the mechanisms and theory of ocean response to TCs (Hong et al., 2022; Zhang 2023). The dataset has the potential for further studies in these fields and can be used for other fields, such as data reanalysis and assimilations.

Author Contributions. The dataset is made and the whole manuscript is written by HZ, the whole observation project is designed by DC, the flow of the manuscript is revised by TL and DT, the dataset is optimized by MH, QL, and JL.

Competing Interests. The contact author has declared that none of the authors has any competing interests.

Financial support. This work has been supported by the National Key R&D Program of China (2023YFF0805300), the Key R&D Program of Zhejiang Province (2024C03257), the Scientific Research Fund of the Second Institute of Oceanography, MNR (JG2309, QNYC2401), the Project supported by Innovation Group Project of Southern Marine Science and Engineering

Guangdong Laboratory (Zhuhai) (316323005), the National Natural Science Foundation of China (42227901, 42176015, 42106008), the National Basic Research Program of China (2013CB430300), the Project supported by Southern Marine Science and Engineering Guangdong Laboratory (Zhuhai) (SML2021SP207, SML2021SP102, SML2022SP401), the MEL Visiting Fellowship (MELRS2303), the Zhejiang Provincial Natural Science Foundation of China (LY24D060003), and the Global Change and Air-Sea Interaction II Program (GASI-01-WPAC-STspr), the Open Project of Fujian Provincial Meteorological Administration (2022K02), and the Zhejiang Provincial Natural Science Foundation of China (2022J011078). This research is also supported by the Key Laboratory of Polar Atmosphere-ocean-ice System for Weather and Climate, Ministry of Education, as well as the CMA-FDU Joint Laboratory of Maine Meteorology.

References

Alford, M. H., Peacock, T., MacKinnon, J. A., Nash, J. D., Buijsman, M. C., Centurioni, L. R., Chao, S. Y., Chang, M. H., Farmer, D. M., Fringer, O. B., Fu, K. H., Gallacher, P. C., Graber, H. C., Helfrich, K. R., Jachec, S. M., Jackson, C. R., Klymak, J. M., Ko, D. S., Jan, S., Johnston, T. M., Legg, S., Lee, I. H., Lien, R. C., Mercier, M. J., Moum, J. N., Musgrave, R., Park, J. H., Pickering, A. I., Pinkel, R., Rainville, L., Ramp, S. R., Rudnick, D. L., Sarkar, S., Scotti, A., Simmons, H. L., St Laurent, L. C., Venayagamoorthy, S. K., Wang, Y. H., Wang, J., Yang, Y. J., Paluszkiewicz, T., and Tang, T. Y.: The formation and fate of internal waves in the South China Sea, Nature, 521, 65–69, doi:10.1038/nature14399, 2015.

Cai, Z., Gan, J., Liu, Z., Hui, C. R., and Li, J.: Progress on the formation dynamics of the layered circulation in the South China Sea, Prog. Oceanogr, 181, 102246, doi:10.1016/j.pocean.2019.102246, 2020.

Chen, W., Hu, P., and Huangfu, J.: Multi-scale climate variations and mechanisms of the onset and withdrawal of the South China Sea summer monsoon, Sci. China Earth Sci., 65, 1030–1046, doi:10.1007/s11430-021-9902-5, 2022.

Chen, W., Zhang, R., Wu, R., Wen, Z., Zhou, L., Wang, L., Hu, P., Ma, T., Piao, J., Song, L., Wang, Z., Li, J., Gong, H., Huangfu, J., and Liu, Y.: Recent Advances in Understanding Multi-scale Climate Variability of the Asian Monsoon, Adv. Atmos. Sci., 40, 1–28, doi:10.1007/s00376-023-2266-8, 2023.

Guan, S., Jin, F. F., Tian, J., Lin, II, Pun, I. F., Zhao, W., Huthnance, J., Xu, Z., Cai, W., Jing, Z., Zhou, L., Liu, P., Zhang, Y., Zhang, Z., Zhou, C., Yang, Q., Huang, X., Hou, Y., and Song, J.: Ocean internal tides suppress tropical cyclones in the South China Sea, Nat. Commun., 15, 3903, doi:10.1038/s41467-024-48003-y, 2024.

He, Y., Lin, X., Han, G., Liu, Y., and Zhang, H.: The different dynamic influences of Typhoon Kalmaegi on two pre-existing anticyclonic ocean eddies, Ocean Sci., 20, 621–637, doi:10.5194/os-20-621-2024, 2024.

Hong, W., Zhou, L., Xie, X., Zhang, H., and Liang, C.: Modified parameterization for near-inertial waves, Acta Oceanol. Sin., 41, 41-53, doi:10.1007/s13131-022-2012-6, 2022.

Jilan, S.: Overview of the South China Sea circulation and its influence on the coastal physical oceanography outside the Pearl River Estuary, Cont. Shelf Res., 24, 1745–1760, doi:10.1016/j.csr.2004.06.005, 2004.

Li, J., Zhou, C., Li, M., Zheng, Q., Li, M., and Xie, L.: A case study of continental shelf waves in the northwestern South China Sea induced by winter storms in 2021, Acta Oceanol. Sin., 43, 59–69, doi:10.1007/s13131-023-2150-5, 2024.

Lim Kam Sian, K. T. C., Dong, C., Liu, H., Wu, R., and Zhang, H.: Effects of Model Coupling on Typhoon Kalmaegi (2014) Simulation in the South China Sea, Atmosphere, 11, 432, doi:10.3390/atmos11040432, 2020.

Lin, J., Fang, S., Xu, W., Ni, S., Zhang, H., and Yang, T.: Multi-instrument observations of microseisms generated by typhoon

Kalmaegi (2014) over the Northwestern Pacific, Earth Planet. Sci. Lett., 594, 117746, doi:10.1016/j.epsl.2022.117746, 2022.

Liu, L., Wang, G., Zhang, Z., and Wang, H.: Effects of drag coefficients on surface heat flux during Typhoon Kalmaegi (2014), Adv. Atmos. Sci., 39, 1501-1518, doi:10.1007/s00376-022-1285-1, 2022.Liu, F., Zhang, H., Ming, J., Zheng, J., Tian, D., and Chen, D.: Importance of Precipitation on the Upper Ocean Salinity Response to Typhoon Kalmaegi (2014), Water, 12, 614, doi:10.3390/w12020614, 2020.

Liu, F., Toumi, R., Zhang, H., Chen, D.: Impact of Precipitation on Ocean Responses during Tropical Cyclone. J. Phys. Oceanogr., 54, 895–909, doi:10.1175/jpo-d-23-0138.1, 2024.

Liu, Q., Kaneko, A., and Jilan, S.: Recent Progress in Studies of the South China Sea Circulation, J. Oceanogr., 64, 753–762, doi:10.1007/s10872-008-0063-8, 2008.

Liu, S.-S., SUN, L., Wu, Q., and Yang, Y.-J.: The responses of cyclonic and anti-cyclonic eddies to typhoon forcing: the vertical temperature-salinity structure changes associated with the horizontal convergence/divergence, J. Geophys. Res. Oceans, 122, 4974–4989, doi:10.1002/2017JC012814, 2017.

Lu, X., Dong, C., Xu, Z., Yang, J., Zhang, H., Wang, D., and Chen, D.: Effects of numerical model's horizontal resolution on the vertical transport of near-inertial energy, Deep-Sea Res. II, 207, 105223, doi:10.1016/j.dsr2.2022.105223, 2023.

Lu, X., Yu, H., Ying, M., Zhao, B., Zhang, S., Lin, L., Bai, L., and Wan, R.: Western North Pacific Tropical Cyclone Database Created by the China Meteorological Administration, Adv. Atmos. Sci., 38, 690–699, doi:10.1007/s00376-020-0211-7, 2021.

Lu, X., Dong, C., Zhang, H., Lim Kam Sian, K. T. C., Yang, J., Xu, Z., Li, G., Wang, Q., Cao, Q., You, Z., and Sommeria, J.: Observational Analysis of Vertical Heat Flux Caused by Typhoon-Induced Near-Inertial Waves Under the Modulation of Mesoscale Eddies, J. Geophys. Res. Oceans, 129, e2024JC021053, doi:10.1029/2024jc021053, 2024.

Ma, Z., Fei, J., Lin, Y., and Huang, X.: Modulation of Clouds and Rainfall by Tropical Cyclone's Cold Wakes, Geophys. Res. Lett., 47, e2020GL088873, doi:10.1029/2020gl088873, 2020.

Nan, F., Xue, H., and Yu, F.: Kuroshio intrusion into the South China Sea: A review, Prog. Oceanogr., 137, 314–333, doi:10.1016/j.pocean.2014.05.012, 2015.

Qi, M., Han, B., Yang, Q., Wu, R., Liu, C., Zhang, G., Zhang, X., Zhou, H., Chen, J., and Chen, D.: Sea Surface Energy Fluxes' Response to the Quasi-Biweekly Oscillation: A Case Study in the South China Sea, Geophys. Res. Lett., 50, doi:10.1029/2023gl104288, 2023.

Quan, Q., Liu, Z., Yang, Y., Cai, Z., Zhang, H., and Liu, X.: Characterization of intraseasonal fluctuations in the abyssal South China Sea: An insight into the energy pathway, Prog. Oceanogr., 206, 102829, doi: 10.1016/j.pocean.2022.102829, 2022.

Shan, K., Chu, P.-S., and Yu, X.: Interdecadal Change of Tropical Cyclone Translation Speed during Peak Season in South China Sea: Observed Evidence, Model Results, and Possible Mechanism, J. Clim., 36, 4531–4541, doi:10.1175/jcli-d-22-0704.1, 2023.

Song, X., Wang, X., Cai, W., and Xie, X.: Observed Air–Sea Turbulent Heat Flux Anomalies during the Onset of the South China Sea Summer Monsoon in 2021, Mon. Weather Rev., 151, 2443–2464, doi:10.1175/mwr-d-22-0314.1, 2023.

Tan, K., Xie, L., Bai, P., Zheng, Q., Li, J., Xu, Y., and Li, M.: Modulation Effects of Mesoscale Eddies on Sea Surface Wave Fields in the South China Sea Derived From a Wave Spectrometer Onboard the China-France Ocean Satellite, J. Geophys. Res. Oceans, 128, doi:10.1029/2021jc018088, 2023.

Wang, Q., Zhang, B., Zeng, L., He, Y., Wu, Z., and Chen, J.: Properties and Drivers of Marine Heat Waves in the Northern South China Sea, J. Phys. Oceanogr., 52, 917–927doi:10.1175/jpo-d-21-0236.1, 2022.

Wang, Q., Zeng, L., Shu, Y., Li, J., Chen, J., He, Y., Yao, J., Wang, D., and Zhou, W.: Energetic Topographic Rossby Waves in the northern South China Sea, J. Phys. Oceanogr., 49, 2697–2714, doi:10.1175/JPO-D-18-0247.1, 2019.

Wu, R., Zhang, H., and Chen, D.: Effect of Typhoon Kalmaegi (2014) on northern South China Sea explored using Muti-

platform satellite and buoy observations data, Prog. Oceanogr., 180, 102218, doi:10.1016/j.pocean.2019.102218, 2020.

Xie, X., Liu, Q., Zhao, Z., Shang, X., Cai, S., Wang, D., and Chen, D.: Deep Sea Currents Driven by Breaking Internal Tides on the Continental Slope, Geophys. Res. Lett., 45, 6160–6166, doi:10.1029/2018GL078372, 2018.

Yang, Y., Wang, D., Wang, Q., Zeng, L., Xing, T., He, Y., Shu, Y., Chen, J., and Wang, Y.: Eddy-Induced Transport of Saline Kuroshio Water Into the Northern South China Sea, J. Geophys. Res. Oceans, 124, 6673–6687, doi:10.1029/2018jc014847, 2019.

Ying, M., Zhang, W., Yu, H., Lu, X., Feng, J., Fan, Y., Zhu, Y., and Chen, D.: An Overview of the China Meteorological Administration Tropical Cyclone Database, J. Atmos. Oceanic Tech., 31, 287–301, doi:10.1175/jtech-d-12-00119.1, 2014.

Zhang, H.: Modulation of Upper Ocean Vertical Temperature Structure and Heat Content by a Fast-Moving Tropical Cyclone, J. Phys. Oceanogr., 53, 493–508, doi:10.1175/JPO-D-22-0132.1, 2023.

Zhang, H., Chen, D., Tongya, L., Tian, D., He, M., Li, Q., Wei, G., and Liu, J.: A Moored Array Observation Dataset for Air-Sea·Surface, Upper and Bottom Ocean in the Northern South China Sea during 2014-2015 (MASCS 1.0) [Data set]. Zenodo. doi: 10.5281/zenodo.13925651, 2024.

Zhang, H., Chen, D., Zhou, L., Liu, X., Ding, T., and Zhou, B.: Upper ocean response to typhoon Kalmaegi (2014), J. Geophys. Res. Oceans, 121, 6520–6535, doi:10.1002/2016jc012064, 2016.

Zhang, H., Liu, X., Wu, R., Chen, D., Zhang, D., Shang, X., Wang, Y., Song, X., Jin, W., Yu, L., Qi, Y., Tian, D., and Zhang, W.: Sea surface current response patterns to tropical cyclones, J. Marine Syst., 208, 103345, doi:10.1016/j.jmarsys.2020.103345, 2020.

Zhang, H., Wu, R., Chen, D., Liu, X., He, H., Tang, Y., Ke, D., Shen, Z., Li, J., Xie, J., Tian, D., Ming, J., Liu, F., Zhang, D., and Zhang, W.: Net Modulation of Upper Ocean Thermal Structure by Typhoon Kalmaegi (2014), J. Geophys. Res. Oceans, 123, 7154–7171, doi:10.1029/2018JC014119, 2018.